Segmentation of Multiple Heart Cavities in 3-D Transesophageal Ultrasound Images

Alexander Haak, Gonzalo Vegas-Sánchez-Ferrero, *Member, IEEE*, Harriët W. Mulder, Ben Ren, Hortense A. Kirişli, Coert Metz, Gerard van Burken, Marijn van Stralen, Josien P. W. Pluim, *Member, IEEE*, Antonius F. W. van der Steen, *Fellow, IEEE*, Theo van Walsum, *Member, IEEE*, and Johannes G. Bosch, *Member, IEEE*

Abstract—Three-dimensional transesophageal echocardiography (TEE) is an excellent modality for real-time visualization of the heart and monitoring of interventions. To improve the usability of 3-D TEE for intervention monitoring and catheter guidance, automated segmentation is desired. However, 3-D TEE segmentation is still a challenging task due to the complex anatomy with multiple cavities, the limited TEE field of view, and typical ultrasound artifacts. We propose to segment all cavities within the TEE view with a multi-cavity active shape model (ASM) in conjunction with a tissue/blood classification based on a gamma mixture model (GMM). 3-D TEE image data of twenty patients were acquired with a Philips X7–2t matrix TEE probe. Tissue probability maps were estimated by a two-class (blood/tissue) GMM. A statistical shape model containing the left ventricle, right ventricle, left atrium, right atrium, and aorta was derived from computed tomography angiography (CTA) segmentations by principal component analysis. ASMs of the whole heart and individual cavities were generated and consecutively fitted to tissue probability maps. First, an average whole-heart model was aligned with the 3-D TEE based on three manually indicated anatomical landmarks. Second, pose and shape of the whole-heart ASM were fitted by a weighted update scheme excluding parts outside of the image sector. Third, pose and shape of ASM for individual heart cavities were initialized by the previous whole heart ASM and updated in a regularized manner to fit the tissue probability maps. The ASM segmentations were validated against manual outlines by two observers and CTA derived segmentations.

Dice coefficients and point-to-surface distances were used to determine segmentation accuracy. ASM segmentations were successful in 19 of 20 cases. The median Dice coefficient for all successful segmentations versus the average observer ranged from 90% to 71% compared with an inter-observer range of 95% to 84%. The agreement against the CTA segmentations was slightly lower with a median Dice coefficient between 85% and 57%. In this work, we successfully showed the accuracy and robustness of the proposed multi-cavity segmentation scheme. This is a promising development for intraoperative procedure guidance, e.g., in cardiac electrophysiology.

I. Introduction

THREE-DIMENSIONAL ultrasound is becoming more and more important for monitoring minimally invasive interventions. Currently, 3-D ultrasound is the only feasible modality which would allow real-time 3-D monitoring of interventions [1]. Compared with transthoracic echocardiography, transesophageal echocardiography (TEE) is especially attractive for cardiac interventions because of its superior image quality and stable, nonobstructive, externally controllable position of the transducer within the esophagus. In particular, 3-D TEE allows direct real-time visualization of the complex 3-D anatomy of the different heart cavities, valves, and the relative position of catheters and closure devices, etc. The transducer is close to the heart, showing important structures such as valves with high resolution, without image deterioration by the chest wall, ribs, and lungs. However, because the transducer is so close, the TEE field of view (FoV) is limited, allows only a partial image of several heart cavities, and is highly dependent on probe manipulation. TEE imaging of the whole heart is mostly impossible. Therefore, image interpretation requires expertise and automated segmentation of 3-D TEE data, which is still challenging [2]. For procedure guidance, the 3-D TEE image should ideally be placed within a model of the heart, allowing navigational help at a multitude of intervention sites. To this end, we propose a cardiac 3-D multi-cavity model automatically fitted within the TEE FoV. This forms the basis for an automatic relative positioning of the image, as well as an automated segmentation of the cavities. This can be used in support of cardiac electrophysiology interventions, e.g., to allow accurate navigation of catheters. Cardiac electrophysiology (EP) concerns the treatment

of conduction and rhythm disorders of the heart. It is a field of rapidly increasing importance within cardiology [3], [4]. During EP interventions, the source of the conduction abnormality is located and treated by tissue ablation. First, position-sensing catheters are used to create a 3-D electro-anatomical map (EAM) of the surface of a heart cavity, e.g., the left atrium (LA). By positioning the tip at a large number of locations on the cavity wall and recording the local ECG signal and 3-D position, a 3-D map of the cavity with its conduction pattern is created. This is a lengthy process with imprecise results. The EAM is rendered in an EP guidance system (e.g., Carto 3 (Biosense Webster, Diamond Bar, CA, USA) or Ensite Velocity (St. Jude Medical, St. Paul, MN, USA), with the positions of all tracked catheters, to guide the intervention. Next, an ablation catheter is navigated to the erroneous conduction sites and tissue is ablated to restore a normal conduction pattern. This requires a precise visualization of the anatomical structures. However, the EAM is imprecise and not detailed. Several approaches have been introduced to improve this guidance. Preoperative CT and MR data have been used, from which several heart cavities are segmented and the surfaces imported into the guidance system [5]. However, such preoperative images often fail to improve the EAM because the CT/MR images are generally taken weeks in advance, which may lead to considerable changes in the anatomy or physiological state. Moreover, the CT/MR images are in different coordinate frames, which makes a registration necessary. Ideally, the 3-D TEE ultrasound data should be segmented and anatomical structures and catheters identified for representation in the interventional guidance system. This could both be done on preoperatively acquired 3-D TEE (for creating a preoperative anatomical map without the need for CT or MR) or on live intraoperative 3-D TEE, to allow live guidance of the catheter positions with respect to true anatomy and EAM. Our proposed approach is the foundation of such applications.

Segmentation of ultrasound images in general is a challenging task [6]. The characteristic speckle structure of an ultrasound image precludes simple separation of different tissues. The images are anisotropic, inhomogeneous in gray level amplitude, and very dependent on probe positioning. Furthermore, ultrasound suffers quite often from artifacts such as echo dropouts and shadowing due to poor probe contact, air bubbles, and calcifications.

Many models have been described for the speckle statistics of the backscattered ultrasound RF-data (gray level amplitude) [7], [8]. Most of the theoretical work has been focused on modeling raw RF data, neglecting all the proprietary postprocessing steps of commercial ultrasound scanners. However, empirical fitting of different distributions to log-compressed [9] and uncompressed [10] gray level data revealed that the Gamma distribution fits such data quite well.

In cardiac ultrasound, segmentation is even more challenging because multiple (incomplete) structures are involved, which have a complex and highly time-variable

shape, and there is a substantial anatomical and pathological variability over the population [6], [11]. Whereas many approaches have been presented for automated segmentation of the left ventricle in transthoracic 3-D echocardiograms [11]–[13], especially for the left ventricle, there are few approaches for 3-D TEE segmentations [2], [14]. The segmentation approach we present meets the following requirements: it deals with ultrasound peculiarities, partially missing information, anatomical variability, and multiple complex structures. We propose a multi-object active shape model (ASM) [15] for this. ASMs are based on statistical shape models and describe the shape variation of a population of shapes using principal component analysis (PCA). This allows the model to generate any shape in the population plus any plausible intermediate or extrapolated form. They are also known to handle missing data very well [16]. Multiple interrelated objects and multidimensional shapes are handled in a natural way.

We present and evaluate an active shape model segmentation method for 3-D TEE, which uses a multi-cavity shape model in conjunction with a blood/tissue classifier based on gamma mixture models (GMM) of gray level amplitudes. To our knowledge, this is the first time a multi-cavity ASM was used in combination with a GMM tissue classifier. For all patients, TEE and computed tomography angiography (CTA) images were acquired, and manual outlines were created in the TEE images by two observers. These were compared with the ASM and TEE segmentations. We also automatically segmented the CTA images by a well-established atlas-based method [17]. We registered the results to the TEE segmentations to compare the results within the TEE sector and also to investigate extrapolation of the heart chambers outside the sector. Furthermore, comparing the registered CTA segmentations with the manual outlines may give some insight into how well the segmentations from the different modalities agree, which is important because the physical image formation principle, segmentation method, acquisition time, and coordinate frame are different. We previously demonstrated a preliminary version of our method on a small data set [18], [19]. In this paper we present our method in detail and evaluate it on a data set of 20 patients.

II. Methodology

A. Gamma Mixture Model

Segmentation in echocardiograms is generally complicated by speckle noise. Ultrasound images naturally exhibit local gray level variations (speckle) due to sound scattering by randomly distributed sub-resolution scatterers. This leads to the typical noisy speckle images that may have a locally poor definition of edges. Using only the local gray level information to find the borders of the different heart chambers usually renders inaccurate segmentations.

The ultrasound speckle statistics depend on many parameters of the medium (scatterer size/density, attenuation, heterogeneity, etc.) and parameters of the ultrasound system (resolution cell dimension, frequency and bandwidth, interpolation, compression, etc.). Classical approaches make use of the assumption of a high number of scatterers per resolution cell which will lead to Rayleigh and Rice distributions. However, modeling the speckle distribution after all processing steps in commercial scanners is difficult because there are many nonlinear processing steps such as adaptive filtering and log-compression. Vendors usually do not disclose the parameters of their processing pipeline. Some researchers have empirically compared the fit of different types of distributions to log-compressed gray level data [9] and to linearly processed RF envelope data [10]. They have shown that the Gamma distribution fits both types of data well. Previously, Vegas-Sánchez-Ferrero *et al.* [20], [21] showed that GMM models the gray level distribution of ultrasound images after beam-forming, postprocessing, and interpolation in an accurate and effective way. Therefore, we decided to use a GMM to describe the speckle distribution of our log-compressed gray level data. [9], [10], [21].

For estimating the likelihood of a region being blood or tissue, a two-class mixture model is used. We consider the voxel gray levels of an image region as an identically distributed random variable:

$$\mathbf{X} = \{X_i\}, \quad 1 \le i \le N, \tag{1}$$

where N denotes the number of voxels in the region considered. The probability density function[1] p of such a mixture model is given by

$$p(x \mid \boldsymbol{\Theta}) = \sum_{j=1}^{2} \pi_j f_X(x \mid \alpha_j, \beta_j), \tag{2}$$

where the vector $\boldsymbol{\Theta}$ holds the parameters for both classes $j = [1,2]$ of the model (π_1, π_2, α_1, β_1, α_2, β_2) and f_X denotes the gamma density function [20] with parameters α and β. The weighting terms π_j stand for the prior probabilities of each class $\pi_j = P(\text{class} = j)$, and thus, the condition $\sum_{j=1}^{2} \pi_j = 1$ holds. The parameters in Θ can easily be estimated with the expectation-maximization algorithm [22].

An example histogram of the gray levels and the fitted GMM with the blood and tissue class are shown in Fig. 1. Please note that the GMM models the empirical distribution quite well. On all patient histograms and fitted GMMs, we computed a Kolmogorov-Smirnov metric of 0.013 ± 0.004 (mean $\pm$ standard deviation). Furthermore, we computed the Kullback-Leibler divergence [20], [23] for all data sets, which was on average 0.03 ± 0.01 (mean $\pm$ standard deviation). Both metrics support our assump-

[1] Please note that we use lowercase p for indicating probability density functions (pdf) and capital P for probabilities.
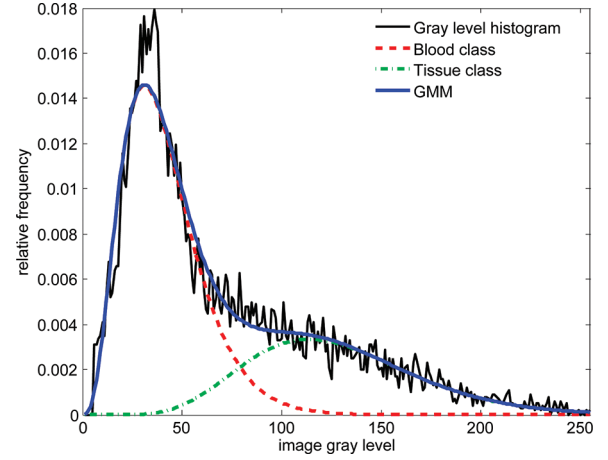

Fig. 1. The GMM (blue solid line) fitted to the log-compressed gray level histogram (black solid line). Grey levels smaller than 5 were discarded to remove areas outside the imaging cone. A k-means ($k = 2$) classifier was used to initialize the GMM. The blood (red dashed line), and tissue (green dashed line) classes are shown in the plot as well. We computed for this example a Kullback-Leibler divergence of 0.025 and a Kolmogorov-Smirnov metric of 0.015, which both support the suitability of using the GMM to model the log-compressed gray level distributions [20], [23].

tion that the log-compressed gray level distributions can be modeled adequately with the GMM.

Finally, probability maps of voxels belonging to blood or tissue ($k = 1, 2$, respectively) are computed using Bayes' theorem:

$$p_k(x \mid \Theta) = \frac{\pi_k f_X(x \mid \alpha_k, \beta_k)}{\sum_{j=1}^{2} \pi_j f_X(x \mid \alpha_j, \beta_j)}. \tag{3}$$

An example 3-D ultrasound volume and the computed tissue probability map are shown in Fig. 2.

B. Active Shape Model

An active shape model [24] represents any shape, $\mathbf{s}$, in a population as the average shape $\bar{\mathbf{s}}$ plus a linear combination of the principal modes of variation, which are described by the eigenvector matrix Φ and the corresponding coefficients $\mathbf{b}$,

$$\mathbf{s} = \bar{\mathbf{s}} + \Phi \mathbf{b}, \tag{4}$$

where $\mathbf{s}$ contains the n 3-D vertices of the shape $\mathrm{s} = (x_1, y_1, z_1, ..., x_n, y_n, z_n)^T$. Usually, the smaller modes of shape variation are removed from the model to suppress noise and to reduce the dimensionality of the model. The ASM used in this work was derived from 151 CTA segmentations [17], [25] containing the left and right ventricle (LV and RV), left and right atria (LA and RA), and the aorta (Ao). The CTA scans were made from a mixed population of patients presenting a large variability in anatomy and pathology [25]. The mean shape of the ASM is shown in
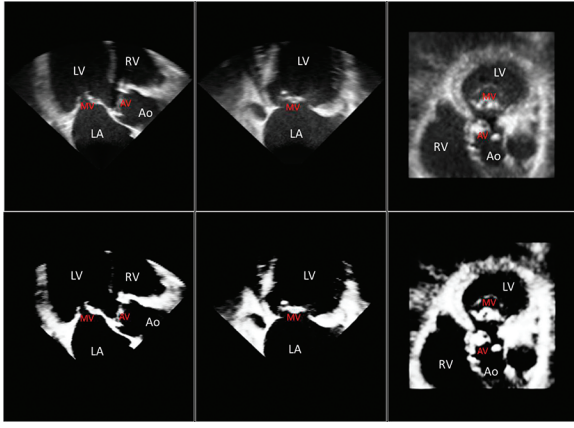
Fig. 2. Three orthogonal cross sections through a TEE volume (top) and the corresponding tissue probability map (bottom). Note the reduction in speckle of the tissue probability map compared with the gray level map.

Fig. 3 and consists of about 10^4 3-D vertices. ASM segmentation is achieved by initializing the shape model at a certain position in the image and finding new candidate points in the neighborhood of the shape. The pose and shape of the ASM is then iteratively estimated (by back-projecting the new shape on the model) until the ASM converges. Update points ($\mathbf{r}'$) are found along the surface normals by minimizing an objective function as described by van Ginneken *et al.* [26], which gives a robust estimator of the blood-tissue transition point. We adopted this approach because we use a CTA-derived ASM and therefore cannot model the TEE gray level or probability map profiles along the surface normals. A weighted least square scheme is used to estimate the pose ($T(a_i, \boldsymbol{\theta}_i, \mathbf{t}_i)$, with a_i being the scale, $\boldsymbol{\theta}_i$ being the Euler angles, and $\mathbf{t}_i$ being the translation at the iteration i [27], [28]) and the shape parameter ($\mathbf{b}'_i$) for each iteration, similarly to the way it was described by Cootes *et al.* [29], which gives for the new shape at iteration i,

$$\mathbf{b}'_i = (\Phi^T W \Phi)^{-1} \Phi^T W (\bar{\mathbf{s}} - \mathbf{s}'_i), \qquad (5)$$

where W is a diagonal matrix containing the vertex weights, w, and s_i is the current shape [e.g., the transformed update points $\mathbf{s}'_i = T(a_i, \boldsymbol{\theta}_i, \mathbf{t}_i)\mathbf{r}'$]. The newly found pose and the shape parameters are regularized with c (rotation, translation, shape) and c_a (scale) to prevent pose jumps by erroneous edge responses:

$$a_i = c_a a_{i-1} + (1 - c_a) a'_i, \qquad (6)$$

$$\boldsymbol{\theta}_i = c \boldsymbol{\theta}_{i-1} + (1 - c) \boldsymbol{\theta}'_i, \qquad (7)$$

$$\mathbf{t}_i = c \mathbf{t}_{i-1} + (1 - c) \mathbf{t}'_i, \text{ and} \qquad (8)$$

$$\mathbf{b}_i = c \mathbf{b}_{i-1} + (1 - c) \mathbf{b}'_i, \qquad (9)$$

where $'$ denotes the estimated unregularized pose and shape parameters at the iteration i.

The vertex weighting factor w consists of a GMM-based edge probability $w_{\text{GMM}}(\mathbf{r}')$, a model distance term
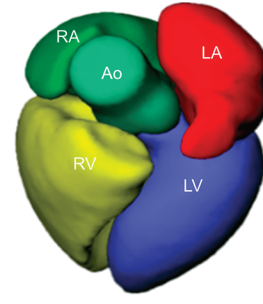

Fig. 3. Mean shape of the multi-cavity statistical shape model [25].

$w_{\text{ASM}}(\mathbf{r}')$, and a term penalizing points outside or close to the border of the pyramidal TEE volume $w_{\text{US}}(\mathbf{r}')$. The weighting factor is computed as follows:

$$w(\mathbf{r}') = w_{\text{ASM}}(\mathbf{r}') \, w_{\text{US}}(\mathbf{r}') \, w_{\text{GMM}}(\mathbf{r}'), \qquad (10)$$

where

$$w_{\text{ASM}}(\mathbf{r}') = \exp\left(-\frac{(||\mathbf{r} - \mathbf{r}'||)^2}{\sigma^2}\right). \qquad (11)$$

The parameter σ defines the range of the model distance penalty term and $||$ indicates the Euclidian distance. The term $w_{\text{US}}(\mathbf{r}')$ is derived by convolving the binary TEE mask with an isotropic Gaussian kernel with a standard deviation of the $\sqrt{20}$ voxel. The GMM term, $w_{\text{GMM}}(\mathbf{r}')$, enhances update points being close to the blood/tissue transition zone (probability of 0.5) and is defined as

$$w_{\text{GMM}}(\mathbf{r}') = 1 - \frac{|p_2(I(\mathbf{r}') \mid \Theta) - 0.5|}{0.5}, \qquad (12)$$

where $I(\mathbf{r}')$ is the local gray level in the TEE image at $\mathbf{r}'$ and $p_2(I(\mathbf{r}')|\Theta)$ stands for the tissue pdf.

C. Segmentation Scheme

We use a three-stage segmentation scheme (see Fig. 4) where the model pose is increasingly regularized from stage to stage. The scheme comprises the following stages.

1) First Stage: In the first step, the ASM of the entire heart containing all cavities ($\text{ASM}_{\text{total}}$) is used. The mean shape ($\bar{\mathbf{s}}_{\text{total}}$) of this ASM is initially transformed to the TEE image by a similarity transform T_{init}, which was derived by manually indicating three landmark points in the TEE image (center of mitral valve, center of aortic valve, and LV apex or a point on the LV long axis). The regularization factors, c and c_a, are set to zero.

2) Second Stage: After the initial pose estimation, the pose and shape of $\text{ASM}_{\text{total}}$ are iteratively updated with intermediate regularization. A shape model covering 90% of the shape variation is used. New shape parameters, $\mathbf{b}$, are computed from the update points ($\mathbf{r}'$), and $\mathbf{b}$ is limited
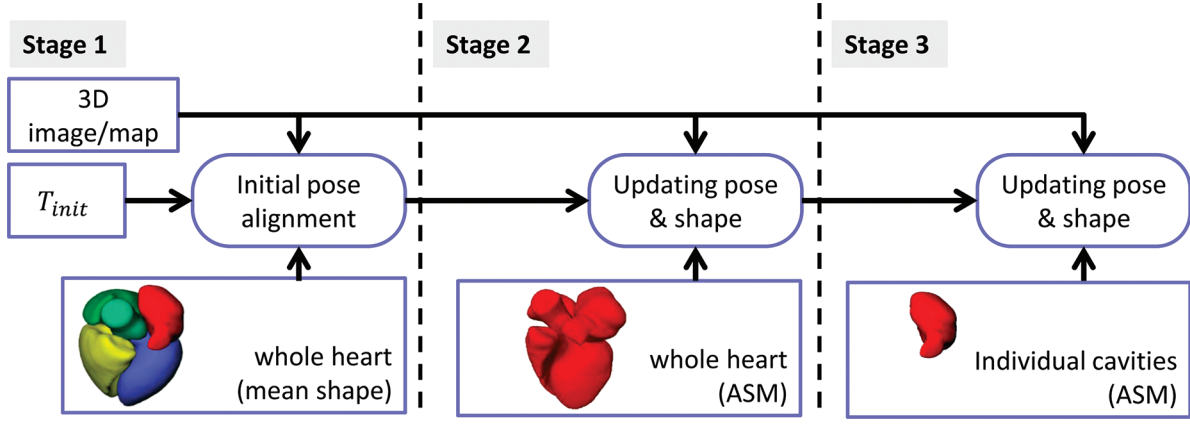
Fig. 4. Three-stage segmentation scheme which adjusts the pose and shape of the model from stage to stage. In the first stage, the mean shape of the entire heart model ($\overline{\mathbf{s}}_{\text{total}}$) is aligned to the TEE volume and the found pose is passed to stage 2. Second, the pose and shape of the complete heart ($\text{ASM}_{\text{total}}$) are updated. In the third stage, individual ASMs for each cavity are fitted to the TEE volume.

to a hyper-ellipsoid ($\mathbf{b}_{\text{lim}}$) by computing the χ^2 distributions and taking the 98% percentiles as the limit [24].

3) Third Stage: In the last stage of the segmentation, for each cavity, a separate shape model covering 98% of the shape variation is used. The pose and shape updates of each ASM are more strongly regularized by setting c to 0.6. The shape updates are again limited to a hyper-ellipsoid, corresponding to the 99.7% percentile.

For all stages, we limit the scale (a_{lim}), the rotation angles ($\boldsymbol{\theta}_{\text{lim}}$), and the translation ($\mathbf{t}_{\text{lim}}$). All limits for the different stages and all other parameters are shown in Table I.

The parameters for the ASM segmentation scheme were empirically chosen based on segmentations of previous data sets.

III. EXPERIMENTS

A. Data

The segmentation method was validated in 3-D TEE data sets obtained from 20 patients (13 male, 7 female; mean age $\pm$ standard deviation: 80 ± 7) undergoing a transcatheter aortic valve implantation (TAVI) in accor-

TABLE I. SEGMENTATION PARAMETERS.

Parameter	Stage 1 (S1)	Stage 2 (S2)	Stage 3 (S3)
c	0.0	0.2	0.6
c_a	0.0	0.2	0.3
σ (voxel)	44	20	20
a_{lim} (%)	± 30 of a_{init}	± 18 of a_{S1}	± 15 of a_{S2}
$\boldsymbol{\theta}_{\text{lim}}$ (°)	± 30 of $\boldsymbol{\theta}_{\text{init}}$	± 20 of $\boldsymbol{\theta}_{\text{S1}}$	± 5 of $\boldsymbol{\theta}_{\text{S2}}$
$\mathbf{t}_{\text{lim}}$ (mm)	± 30 of $\mathbf{t}_{\text{init}}$	± 20 of $\mathbf{t}_{\text{S1}}$	± 5 of $\mathbf{t}_{\text{S2}}$
$\mathbf{b}_{\text{lim}}$ (%)	0.0	98.0	99.7

σ defines the range of w_{ASM}; c regularizes $\boldsymbol{\theta}$, $\mathbf{t}$, and $\mathbf{b}$; and c_a regularizes a at each iteration.
Upper and lower limits for the pose and shape parameters have the subscript lim.

dance with the hospital ethical regulations. The patients all had severe aortic valve stenosis with different severity of valve regurgitation. This caused for many patients severe pathologies with considerable left ventricular and atrial enlargement and hypertrophy. All TAVI patients had 3-D TEE data acquired with a matrix TEE probe (X7–2t, Philips Healthcare, The Netherlands) during the preparation of the intervention. The patients were anesthetized and in supine position. Conventional log-compressed gray level data were used in the study. The sonographer used a preset but was free to adapt the machine parameters image depth (10 ± 2 cm), focus, gain (47 ± 5 dB), compression (49 ± 1%), and time-gain curve to yield the best and most homogeneous image quality for the specific patient. One heart cycle was acquired in live 3-D mode (no stitching of sub-volumes acquired over several cardiac cycles), yielding a frame rate of about 4 ± 1 volumes/s. The power settings were fixed yielding an MI of 0.5 and a TI of 0.1. All patients also underwent a gated CTA for preoperative planning. Usually, 19 time frames were acquired and the ED time frame was selected. The CTA volumes were cropped so that only the heart was in the image volume.

B. Gold Standard and Evaluation of Ground Truth

To provide a segmentation ground truth, 2-D contours of all visible cavities in multiple short and long axis views were manually annotated by two independent observers in all end-diastolic (ED) TEE images. The ED time-frame was manually selected by visual inspection of the mitral valve (closed) and the largest volume (LV). To speed up the manual outline we used the roughly aligned mean shape ($\overline{\mathbf{s}}_{\text{total}}$) as a starting point for the observer outlines. First, one observer indicated four landmark points on the mitral valve (MV) annulus, one on the aortic valve (AV) and one at the apex of the left ventricle. The center of the four MV points, AV, and apex point was then used to compute an initial similarity transform for the mean shape of the total heart model ($\overline{\mathbf{s}}_{\text{total}}$). The mean shape was overlaid on the TEE image, and small adjustments could be

Fig. 5. Example of manual annotation of the heart cavities in 15 slices of a TEE volume.

TABLE II. MEAN DICE COEFFICIENTS AND P2S$_{MEAN}$.

	LV	RV	LA	RA	Ao
Dice inter Obs (%)	91.3	84.2	95.2	83.4	82.7
Dice init ASM (%)	83.3	72.6	67.4	63.4	59.5
Dice final ASM (%)	90.0	79.5	87.4	64.8	70.1
Dice CTA (%)	84.5	74.7	85.3	68.9	61.6
P2S$_{mean}$ inter Obs (mm)	2.56	3.46	1.56	2.76	2.06
P2S$_{mean}$ init ASM (mm)	4.33	6.16	6.85	5.71	4.72
P2S$_{mean}$ ASM (mm)	2.82	5.17	3.10	5.70	3.34
P2S$_{mean}$ CTA (mm)	4.74	6.84	4.62	5.41	5.45

segmentations were compared with the manually defined average observer contours and the CTA segmentations. Because the CTA is in a different coordinate system from the TEE, the two need to be registered first. The obtained CTA and TEE segmentations were rigidly registered using surface-based iterative closest point (ICP, see [32] for more details) alignment, after initial coarse alignment of the heart by registration of the center of gravities of the corresponding cavities.

C. Evaluation Measures

For comparing the different segmentations, overlap in area or volume for each cavity was expressed as a Dice coefficient in 2-D or 3-D, as applicable [33]. The distance between corresponding segmentations was computed as average Euclidean point-to-surface distance. The Dice coefficients of segmented TEE and CTA volumes and the mean point-to-surface distances (P2S$_{mean}$) were calculated within the pyramidal TEE image sector (cropped) as well as for the entire heart volume (complete). Several comparisons were made: first, the comparison of both manual observers to each other gave a measure of inter-observer variability (inter Obs). This served as a baseline for the segmentation performance of the ASM. Second, the comparison of CTA to the average manual observer (ground truth) provided a measure of intermodality differences, registration, and segmentation inaccuracies. Third, the ASM TEE segmentations can be compared with the manual ground truth and to the CTA segmentations points lying within the TEE sector, to evaluate its performance. Fourth, by comparing the ASM cavity parts outside the sector to CTA, one can evaluate the extrapolation capabilities of the ASM. Fifth, by comparing the final ASM segmentation to the initial result, one can evaluate the value of the segmentation scheme. The mean Dice coefficients and distances are also summarized in Table II. Please note that any evaluation measure using the manual outlines was only computed within the FoV.

made to the landmark points to obtain an optimal initial pose of the model. Using this transformation as a starting point, the manual outlining was performed independently by two observers, in eleven 2-D short-axis views and 4 collinear long-axis views, obtained by slicing the TEE image and the mean shape model. The 2-D contours of $\overline{\mathbf{s}}_{total}$ were interpolated by B-splines, and the control points were interactively manipulated by the observers to adapt the contours to the correct borders of the different cavities. Crossing points of contours from the different short- and long-axis planes were displayed in the respective perpendicular planes to ensure 3-D consistency in the manual outlines. Please note that outlines outside the FoV are leftovers from the initialization with the mean model and are not used in any way. Papillary muscles and trabeculations were included in the cavities (excluded from myocardium) as recommended in the ASE guidelines [30]. An example TEE volume with the outlines of one observer is shown in Fig. 5. From the two manual segmentations, an "average observer" segmentation was constructed as the ground truth segmentation. The average observer contour was created by computing for each plane the signed distance map for both observer contours and adding these maps. This produces a map where the average contour is represented by the zero pixel values. The resulting map was thresholded, and the average observer contour points were detected by a fast marching squares scheme [31]. Additionally, CTA images were obtained from the same 20 patients and were segmented in 3-D using the multi-atlas-based approach introduced in [17]. Please note that the used ASM did not include any of these CTA segmentations. For one patient the segmentation failed due to severe pathology. Therefore, we excluded this CTA segmentation from our analyses. The CTA segmentations provide an independent ground truth of the cavity outline. In contrast to the manual TEE segmentations, these are fully 3-D and not limited to the TEE sector. The statistical shape model was derived earlier from 151 CTAs of other patients of mixed pathology [25]. For the evaluation, ASM

IV. RESULTS

The inter-observer-variability Dice coefficients and the P2S$_{mean}$ for all sets and heart cavities are shown in the boxplots of Figs. 6 and 7. The Dice coefficients, and the P2S$_{mean}$ of the average observer to $\overline{\mathbf{s}}_{init}$, to the final segmentation result, and to registered CTA segmentations
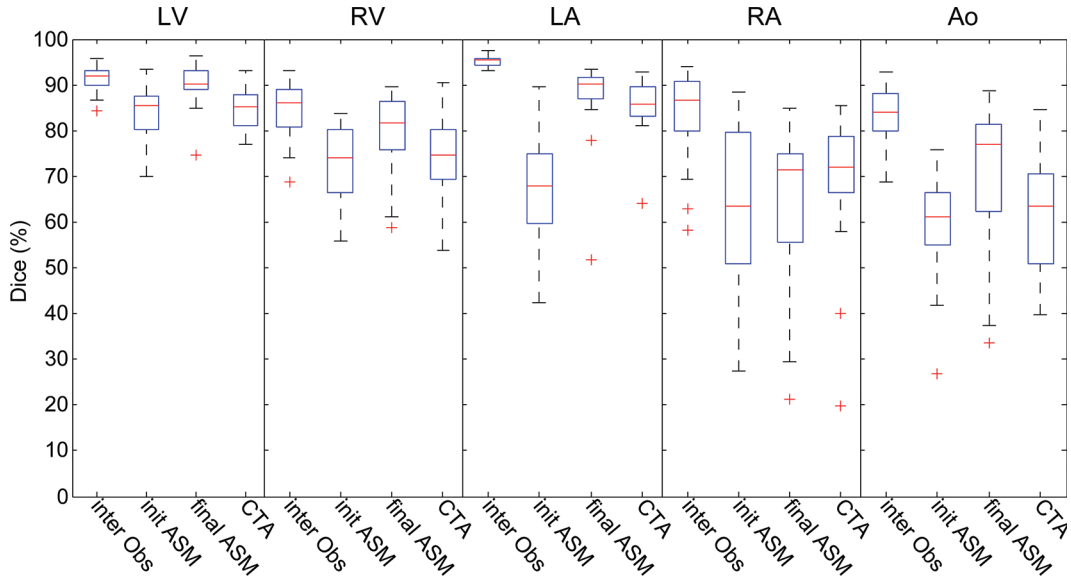
Fig. 6. Dice coefficients for all five heart cavities between average observer (avg Obs) and different segmentations, averaged over all patients. From left to right: observer one versus observer two (inter Obs), avg Obs versus initial model (init ASM), avg Obs versus final ASM TEE segmentation (final ASM), and avg Obs versus the CTA segmentation (CTA). Please note that the Dice coefficient was computed only within the FoV.

are also shown in Figs. 6 and 7. Note that for the left heart chambers (LV and LA) we obtain the best inter-observer variability and also the best segmentation results (final ASM). For the right heart chambers (RV and RA) we have less agreement between the observers, and the ASM segmentation results agree less with the average observer. A qualitative comparison of an ASM segmentation with the two manual observers is shown in Fig. 8.

The Dice coefficients and the $P2S_{mean}$ of the registered CTA segmentation with the average observer for all sets and heart cavities are shown in the boxplots of Figs. 6 and 7 (CTA). Note that generally the agreement between manual outlines and CTA segmentations is less than for the ASM segmentations.

The Dice coefficients and the $P2S_{mean}$ of the registered CTA segmentation with the ASM segmentations for all sets and heart cavities are shown in Figs. 9 and 10.

Note that the agreement of the segmentation for the full heart is only slightly decreased compared with the agreement confined within the FoV of the TEE image sector.

V. DISCUSSION

In this paper, we validated our multi-cavity ASM segmentation method for 3-D TEE on an extended data set of 20 patients. We successfully showed that the proposed
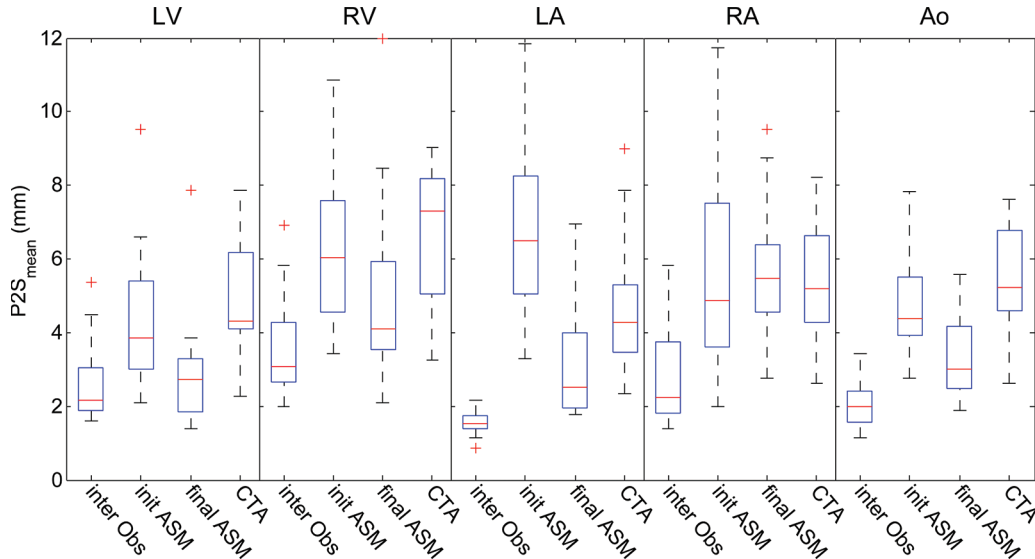

Fig. 7. $P2S_{mean}$ for all five heart cavities between average observer (avg Obs) and different segmentations, averaged over all patients. From left to right: observer one versus observer two (inter Obs), avg Obs versus initial model (init ASM), avg Obs versus final ASM TEE segmentation (final ASM), and avg Obs versus the CTA segmentation (CTA). Please note that the $P2S_{mean}$ was computed only within the FoV.
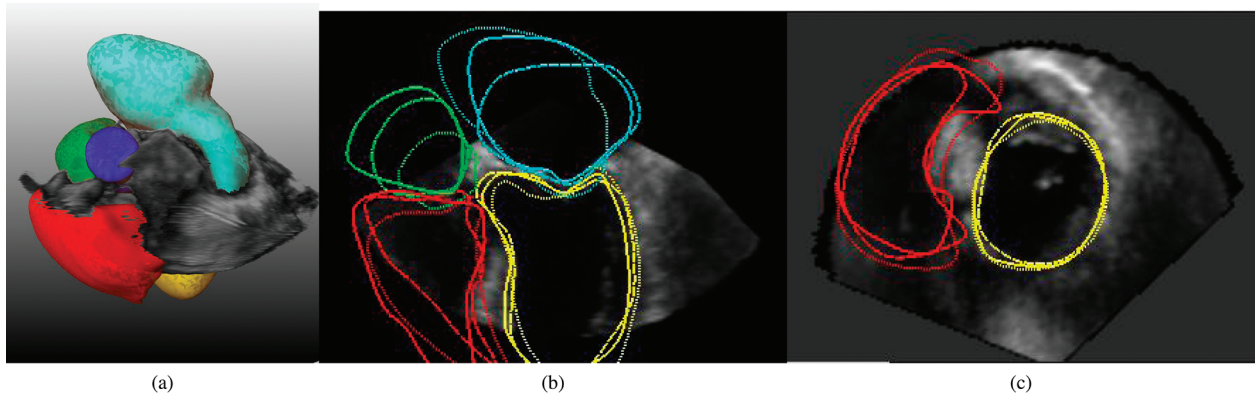
Fig. 8. Qualitative example of a final ASM segmentation within the rendered 3-D TEE volume (a). The left ventricle is shown in yellow, the right ventricle in red, left atrium in cyan, the right atrium in green, and the aorta in blue. Two cross sections are shown in (b) and (c) with contours of the two manual observers (solid and dashed lines) and the final ASM (dotted lines). Note the limited FoV of the TEE probe.

segmentation scheme, using a GMM tissue/blood classifier in conjunction with a multi-cavity ASM, can handle narrow-view data and automatically identify different heart chambers in complex TEE images. The run time of the nonoptimized segmentation scheme was on the order of 2 min for one patient data set.

The accuracy of the segmentation for the different cavities was reasonably close to the inter-observer variability of the manual segmentations that served as ground truth. As expected, the final segmentation had a much higher overlap with the average observer than the initially placed average model for all cavities (see Fig. 6) and the Dice coefficient improved on average by 6.7, 6.9, 20.0, 1.3, and 11.0 percentage points for LV, RV, LA, RA, and Ao, respectively. For the LV and RV, we could achieve segmentation accuracy close to the inter-observer variability even though mostly large parts of the RV and LV were not visible in the TEE image. We also achieved a good segmentation for the LA (the second highest Dice score of all cavities segmented). However, the inter-observer variability of the LA is very low because this part has the best contrast in the image with the sharpest borders and mostly simple anatomy (not much trabeculation). Although the ASM results cannot match this extremely low variability, we still consider our segmentation scheme to provide good

results. The results of the $P2S_{mean}$ support these findings. The LA segmentation may remain suboptimal due to the small visible portion of the LA in the TEE image (only the inferior part is visible) and negative influence of the combined model in previous steps. Specific optimizations of parameters per cavity (step 3) might help here.

The comparison of the ASM segmentations with automatically segmented CTA of the same patients showed good correspondence, which is supported by the obtained Dice coefficients (see Fig. 6). Comparing the correspondence for only the TEE sector with that for the entire heart, we see that the Dice coefficients drop by only a small amount: 6.3, 12.9, 8.9, 5.0, and 6.2 percentage points, which supports that the ASM has good generalization capabilities and can be used to extrapolate the heart cavities to beyond the limited view of the sector with reasonable accuracy. The good agreement of the TEE segmentations with the real anatomical structure can be qualitatively inspected by overlaying the transformed TEE segmentations with the CTA image as shown in Fig. 11.

The patients used in our study were quite different from the normal population with a rather abnormal anatomy (e.g., highly dilated atria) and reduced TEE image quality. Although this might form a challenge for the ASM's statistical shape model coverage, very acceptable segmen-
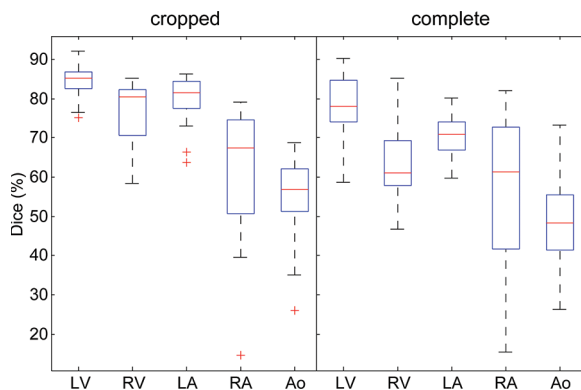

Fig. 9. Dice coefficients of TEE versus CTA segmentations (3-D) considering only the TEE FoV (cropped) or the entire heart (complete).
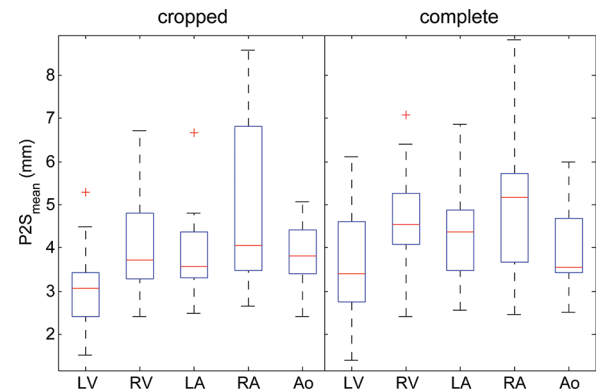

Fig. 10. $P2S_{mean}$ of TEE versus CTA segmentations (3-D) considering only the TEE FoV (cropped) or the entire heart (complete).
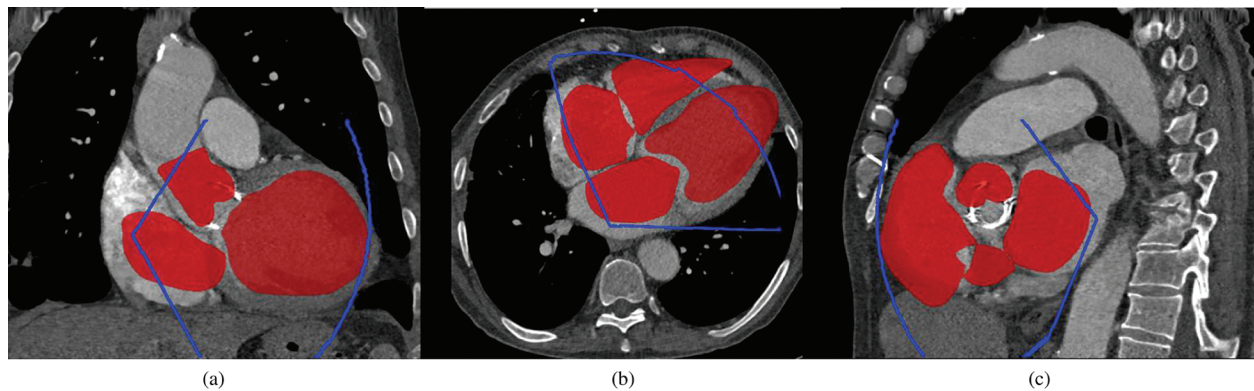
Fig. 11. Qualitative example of a TEE segmentation transformed into the corresponding CTA volume. (a) TEE, (b) GMM, (c) GMM.

tations were still achieved. Only in one case the ASM did not converge: this case had a limited FoV with poor image quality and an indeterminate content. For all other cases, which included a wide range of anatomical variation, image orientations and artifacts, segmentation was successfully converging.

The remaining P2S errors are on the order of 3 to 4 mm for the different cavities. Although this is sufficient for many applications, and better than accuracies of EAM or preoperative imaging in EP, precise interventions may require precisions in the order of 1 to 2 mm. An additional refinement by an alternative or hybrid edge finding might supply this.

Our study has some limitations. The 3-D ASM segmentations were only compared with several 2-D average observer contours, which present a rather coarse sampling of the 3-D structures segmented. However, there is currently no feasible manual ground truth for studies dealing with larger data sets. We tried to overcome this limitation by introducing an alternative ground truth provided by the CTA segmentations. However, the CTA and ASM segmentation needs to be registered, which may bias our results. An image-based registration may overcome this problem, but we are not aware of any robust automatic method. Furthermore, the contrast in CTA image intensities and the detected edges in the GMM (e.g., probability of 0.5) are caused by different physical mechanisms and may differ considerably. Also, there may have been a significant amount of remodeling of the heart anatomy or change in physiological conditions because there were several weeks between the CTA scan and the intervention. In addition, the temporal sampling of the TEE volumes was quite low and may have resulted in mismatches between ASM and CTA segmentations. Furthermore, the starting point of the manual outlines and the initialization of the automatic segmentation was the same. This may have led to a bias during the outlining process. The Dice coefficients and $P2S_{\mathrm{mean}}$ reveal that the initial model is very different from the manual contours and from the final segmentations (see Figs. 6 and 7). Therefore, we feel confident that the bias is minimal. Another limitation is the limited TEE FoV. Even though the segmentation scheme seems to extrapolate the cavities outside the FoV relatively well, we would like to investigate if image fusion of different TEE views will improve the segmentation results.

Several extensions of the current approach are foreseen. Further improvement may be reached by optimizing algorithmic parameters per cavity or adding a final contour refinement stage. An iterated local estimation of blood/tissue probability based on prior local knowledge of blood and tissue from the previous model estimate could be a promising approach. The integration of an automatic landmark detection scheme is a promising extension, which will render our approach into a fully automatic segmentation scheme. Application in EP patients, including models generated from such patients, is a following step.

VI. CONCLUSION

In this work we successfully showed on 20 patient data sets that our segmentation approach is robust and accurate. This whole-heart model segmentation method will provide excellent opportunities for multi-view fusion and instrument tracking in procedure guidance.

ACKNOWLEDGMENTS

REFERENCES

[1] G. Gao, G. Penney, Y. Ma, N. Gogin, P. Cathier, A. Arujuna, G. Morton, D. Caulfield, J. Gill, C. Aldo Rinaldi, J. Hancock, S. Redwood, M. Thomas, R. Razavi, G. Gijsbers, and K. S. Rhode "Registration of 3D trans-esophageal echocardiography to X-ray fluoroscopy using image-based probe tracking," *Med. Image Anal.*, vol. 16, no. 1, pp. 38–49, 2012.

[2] P. Burlina, R. Mukherjee, R. Juang, and C. Sprouse, "Recovering endocardial walls from 3D TEE," in *6th Int. Conf. Functional Imaging and Modeling of the Heart*, 2011, pp. 284–293.

[3] M. W. Rich, "Epidemiology of atrial fibrillation," *J. Interv. Card. Electrophysiol.*, vol. 25, no. 1, pp. 3–8, 2009.

[4] J. Heeringa, D. A. van der Kuip, A. Hofman, J. A. Kors, G. van Herpen, B. H. Stricker, T. Stijnen, G. Y. Lip, and J. C. Witteman,

"Prevalence, incidence and lifetime risk of atrial fibrillation: The Rotterdam study," *Eur. Heart J.*, vol. 27, no. 8, pp. 949–953, 2006.

[5] Z. J. Malchano, P. Neuzil, R. C. Cury, G. Holmvag, J. Weichelt, E. J. Schmidt, J. N. Ruskin, and V. Y. Reddy, "Integration of cardiac CT/MR imaging with three-dimensional electroanatomical mapping to guide catheter manipulation in the left atrium: Implications for catheter ablation of atrial fibrillation," *J. Cardiovasc. Electrophysiol.*, vol. 17, no. 11, pp. 1221–1229, 2006.

[6] J. A. Noble and D. Boukerroui, "Ultrasound image segmentation: A survey," *IEEE Trans. Med. Imaging*, vol. 25, no. 8, pp. 987–1010, Aug. 2006.

[7] C. B. Burckhardt, "Speckle in ultrasound B-mode scans," *IEEE Trans. Sonics Ultrason.*, vol. 25, no. 1, pp. 1–6, Jan. 1978.

[8] R. F. Wagner, S. W. Smith, J. M. Sandrik, and H. Lopez, "Statistics of speckle in ultrasound B-scans," *IEEE Trans. Sonics Ultrason.*, vol. 30, no. 3, pp. 156–163, May 1983.

[9] Z. Tao, H. D. Tagare, and J. D. Beaty, "Evaluation of four probability distribution models for speckle in clinical cardiac ultrasound images," *IEEE Trans. Med. Imaging*, vol. 25, no. 11, pp. 1483–1491, Nov. 2006.

[10] M. M. Nillesen, R. G. P. Lopata, I. H. Gerrits, L. Kapusta, J. M. Thijssen, and C. L. de Korte, "Modeling envelope statistics of blood and myocardium for segmentation of echocardiographic images," *Ultrasound Med. Biol.*, vol. 34, no. 4, pp. 674–680, 2008.

[11] K. Y. Leung and J. G. Bosch, "Automated border detection in three-dimensional echocardiography: Principles and promises," *Eur. J. Echocardiogr.*, vol. 11, no. 2, pp. 97–108, 2010.

[12] D. Barbosa, T. Dietenbeck, B. Heyde, H. Houle, D. Friboulet, J. D'hooge, and O. Bernard, "Fast and fully automatic 3-D echocardiographic segmentation using B-spline explicit active surfaces: Feasibility study and validation in a clinical setting," *Ultrasound Med. Biol.*, vol. 39, no. 1, pp. 89–101, 2013.

[13] M. M. Nillesen, R. G. Lopata, H. J. Huisman, J. M. Thijssen, L. Kapusta, and C. L. de Korte, "Correlation based 3-D segmentation of the left ventricle in pediatric echocardiographic images using radio-frequency data," *Ultrasound Med. Biol.*, vol. 37, no. 9, pp. 1409–1420, 2011.

[14] R. I. Ionasec, I. Voigt, B. Georgescu, Y. Wang, H. Houle, F. Vega-Higuera, N. Navab, and D. Comaniciu, "Patient-specific modeling and quantification of the aortic and mitral valves from 4-D cardiac CT and TEE," *IEEE Trans. Med. Imaging*, vol. 29, no. 9, pp. 1636–1651, 2010.

[15] T. F. Cootes, C. J. Taylor, D. H. Cooper, and J. Graham, "Training models of shape from sets of examples," in *Proc. British Machine Vision Conf.* London, UK: Springer, 1992, pp. 9–18.

[16] N. Baka, B. L. Kaptein, J. E. Giphart, M. Staring, M. de Bruijne, B. P. F. Lelieveldt, and E. R. Valstar, "Evaluation of automated statistical shape model based knee kinematics from biplane fluoroscopy," *J. Biomech.*, vol. 47, no. 1, pp. 122–129, 2014.

[17] H. A. Kirişli, M. Schaap, S. Klein, S. L. Papadopoulou, M. Bonardi, C. H. Chen, A. C. Weustink, N. R. A. Mollet, E. P. A. Vonken, R. J. van der Geest, T. van Walsum, and W. J. Niessen, "Evaluation of a multi-atlas based method for segmentation of cardiac CTA data: A large-scale, multi-center and multi-vendor study," *Med. Phys.*, vol. 37, no. 12, pp. 6279–6291, 2010.

[18] A. Haak, G. Vegas-Sanchez-Ferrero, H. H. Mulder, H. H. Kirisli, N. Baka, C. Metz, S. Klein, B. Ren, G. van Burken, A. F. W. van der Steen, J. P.W. Pluim, T. van Walsum, and J. G. Bosch, "Segmentation of 3D transesophageal echocardiograms by multi-cavity active shape model and gamma mixture model," in *Augmented Reality Environments for Medical Imaging and Computer-Assisted Interventions.* Berlin, Germany: Springer, 2013.

[19] A. Haak, G. Vegas-Sanchez-Ferrero, H. H. Mulder, H. H. Kirişli, N. Baka, C. Metz, S. Klein, B. Ren, G. van Burken, J. P. W. Pluim, A. F.W. van der Steen, T. van Walsum, and J. G. Bosch, "Simultaneous segmentation of multiple heart cavities in 3D transesophageal echocardiograms," in *2013 Joint UFFC, EFTF and PFM Symp.*, 2013, pp. 659–662.

[20] G. Vegas-Sánchez-Ferrero, J. Seabra, O. Rodriguez-Leor, A. Serrano-Vida, S. Aja-Fernández, C. Palencia, M. Martin-Fernandez, and J. Sanches, "Gamma mixture classifier for plaque detection in intravascular ultrasonic images," *IEEE Trans. Ultrason. Ferroelectr. Freq. Control*, vol. 61, pp. 44–61, Jan. 2014.

[21] G. Vegas-Sánchez-Ferrero, M. Martín-Martinez, and J. Miguel Sanches, "A gamma mixture model for IVUS imaging," in *Multi-Modality Atherosclerosis Imaging and Diagnosis*, L. Saba, J. M.

[22] T. K. Moon, "The expectation-maximization algorithm," *IEEE Signal Process. Mag.*, vol. 13, no. 6, pp. 47–60, Nov. 1996.

[23] R. M. Dudley, *Uniform Central Limit Theorems*, 1st Ed. Cambridge, UK: Cambridge University Press, 1999.

[24] T. F. Cootes, D. Cooper, C. J. Taylor, and J. Graham, "Active shape models—Their training and application," *Comput. Vis. Image Underst.*, vol. 61, no. 1, pp. 38–59, 1995.

[25] C. T. Metz, N. Baka, H. A. Kirisli, M. Schaap, S. Klein, L. Neefjes, N. R. A. Mollet, B. P. F. Lelieveldt, M. de Bruijne, W. J. Niessen, and T. van Walsum, "Regression-based cardiac motion prediction from single-phase CTA," *IEEE Trans. Med. Imaging*, vol. 31, no. 6, pp. 1311–1325, 2012.

[26] B. van Ginneken, A. F. Frangi, J. J. Staal, B. M. ter Haar Romeny, and M. A. Viergever, "Active shape model segmentation with optimal features," *IEEE Trans. Med. Imaging*, vol. 21, no. 8, pp. 924–933, aug. 2002.

[27] K. S. Arun, T. S. Huang, and S. D. Blostein, "Least-squares fitting of two 3-D point sets," *IEEE Trans. Pattern Anal. Mach. Intell.*, vol. 9, no. 5, pp. 698–700, Sep. 1987.

[28] B. K. P. Horn, H. M. Hilden, and S. Negahdaripour, "Closed-form solution of absolute orientation using orthonormal matrices," *J. Opt. Soc. Am.*, vol. 5, no. 7, pp. 1127–1135, 1988.

[29] T. F. Cootes, A. Hill, C. J. Taylor, and J. Haslam, "Use of active shape models for locating structures in medical images," *Image Vis. Comput.*, vol. 12, no. 6, pp. 355–365, 1994.

[30] R. M. Lang, M. Bierig, R. B. Devereux, F. A. Flachskampf, E. Foster, P. A. Pellikka, M. H. Picard, M. J. Roman, J. Seward, J. S. Shanewise, S. D. Solomon, K. T. Spencer, M. S. Sutton, and W. J. Stewart, "Recommendations for chamber quantification: A report from the American Society of Echocardiography's Guidelines and Standards Committee and the chamber quantification writing group, developed in conjunction with the European Association of Echocardiography, a branch of the European Society of Cardiology," *J. Am. Soc. Echocardiogr.*, vol. 18, no. 12, pp. 1440–1463, 2005.

[31] W. E. Lorensen and H. E. Cline, "Marching cubes: A high resolution 3D surface construction algorithm," *Comput. Graph.*, vol. 21, no. 4, pp. 163–169, 1987.

[32] P. J. Besl and H. D. McKay, "A method for registration of 3-D shapes," *IEEE Trans. Pattern Anal. Mach. Intell.*, vol. 14, no. 2, pp. 239–256, 1992.

[33] L. R. Dice, "Measures of the amount of ecologic association between species," *Ecology*, vol. 26, no. 3, pp. 297–302, 1945.

Alexander Haak is currently working as a Ph.D. candidate at the Department of Biomedical Engineering, Thoraxcenter, Erasmus MC, Rotterdam. He is interested in ultrasound imaging for intervention guidance, 3-D ultrasound, image reconstruction, segmentation, and instrument tracking. He received his undergraduate degree in applied physics and computer engineering from Merseburg University of Applied Sciences, Germany, in 2007. He obtained his M.S. degree in electrical engineering from the University of Illinois at Urbana-Champaign in 2010. His master's degree research focused on parametric ultrasound imaging for tissue characterization.

Gonzalo Vegas-Sánchez-Ferrero (M'11) received the M.S. degree in telecommunication engineering from the University of Valladolid, Valladolid, Spain, in 2006. In 2006, he joined the Laboratory of Image Processing, University of Valladolid, as a Researcher. In 2013 he received the International Ph.D. degree. He received the Extraordinary Doctorate Award of the University of Valladolid and was a finalist of the best Ph.D. thesis on information technologies and telecommunications of the Official College of Telecommunications Engineering of Spain. He was a Visiting Researcher with the Center for Computational Imaging and Simulation Technologies in Biomedicine, Barcelona, Spain; Instituto Superior Tecnico, Lisboa, Portu-

gal; the Athena Research Team, INRIA, Sophia-Antipolis, France; and the Thoraxcenter, Erasmus MC, Rotterdam. He is a coeditor and/or reviewer of several scientific journals. His research interests include statistical and mathematical methods for image and signal processing. Dr. Vegas-Sánchez-Ferrero was the recipient of an FPI grant from the Spanish Government and is currently an Advanced M+VISION Fellow of the Madrid-MIT Consortium.

Harriët W. Mulder received her M.Sc. degree in medical natural sciences (specialization medical physics) at the VU University, Amsterdam, The Netherlands, in 2010. Since March 2010, she has worked as a Ph.D. degree student at the Image Sciences Institute, University Medical Center Utrecht, in Utrecht. Currently, she is working on the registration and fusion of transesophageal echocardiography (TEE) images.

Ben Ren is a Ph.D. candidate in the department of Cardiology, Thoraxcenter, Erasmus MC, in The Netherlands. Her research topic is 3-D echocardiography in assessing valvular diseases and cardiac functions. She also participates in the "integration of 3-D ultrasound into electrophysiology for support of ablation procedures" project in the Department of Biomedical Engineering, Thoraxcenter, Erasmus MC. She received her M.D. degree at the West China School of Medicine, Sichuan University in China in 2010. Her master's degree research topic in 2010 was 3-D echocardiographic evaluation of the aortic annulus.

Hortense A. Kirişli's photograph and biography were unavailable at the time of publication.

Coert Metz's photograph and biography were unavailable at the time of publication.

Gerard van Burken's photograph and biography were unavailable at the time of publication.

Marijn van Stralen obtained his M.Sc. degree in medical-technical computer science at Utrecht University. He received his Ph.D. degree in medical image analysis on automated analysis of 3-D echocardiography from Leiden University in 2009, working at the Laboratory for Clinical and Experimental Image Processing (LKEB) at the Leiden University Medical Center (2003–2005) and at the Department of Biomedical Engineering of the Erasmus Medical Center in Rotterdam, The Netherlands (2005–2008). Since 2008, he has been working as a postdoctoral researcher on 4-D medical image analysis at the Image Sciences Institute at the University Medical Center in Utrecht, The Netherlands. His work now focuses on MR imaging and its main application is abdominal perfusion imaging.

Josien P. W. Pluim received her M.Sc. degree in computer science (University of Groningen, The Netherlands) in 1996 and a Ph.D. degree (Utrecht University, The Netherlands) in 2001. Her Ph.D. research was performed at the Image Sciences Institute, University Medical Center Utrecht, on mutual information-based image registration. She is currently an associate professor at the Image Sciences Institute, Utrecht. Her research group works on various topics in medical image analysis, in particular for oncology and digital pathology.

Antonius F. W. (Ton) van der Steen (M'94, SM'03, F'13) is a Professor in biomedical engineering in cardiology. He has an M.Sc. degree in applied physics (1989, Technical University Delft) and a Ph.D. degree in medical science (1994, Catholic University Nijmegen). Since 1994 he has been connected to the Thorax Centre and the Interuniversity Cardiology Institute of The Netherlands. He is the head of biomedical engineering of the Thorax Centre, Erasmus MC. Since 2013 he has also been a full professor in applied physics at the Technical University Delft. Since 2014 he has been an honorary visiting professor to the Shenzhen Institutes of Advanced Technologies. His expertise is mainly in diagnostic cardiologic imaging devices with emphasis on echography. Current research interests are focused to vulnerable atherosclerotic plaque detection, ultrasound contrast agents, ultrasound transducers, and vascular biomechanics. His research on vulnerable plaque detection has resulted in many publications and several patents on IVUS flow, IVUS palpography, harmonic IVUS, and vasa vasorum detection. He is a member of the Netherlands Academy of Engineering (AcTI) and a member of the Netherlands Academy of Sciences (KNAW). He is a Fellow of the IEEE and a Fellow of the European Society of Cardiology. He was the IEEE UFFC Distinguished lecturer in 2011–2012.

Theo van Walsum (M'07) graduated in informatics (computer science) at the Delft University of Technology in 1990. In 1995 he received his Ph.D. degree at the Scientific Visualization Group of Delft University of Technology, after which he joined the Laboratorium voor Klinische en experimentele Beeldverwerking (LKEB) at the Leiden University Medical Center, Leiden. In 1996 he held a postdoctoral position at the Image Sciences Institute at UMC Utrecht, where he started working on image guidance applications. Since 2005 he has been working at the Biomedical Imaging Group Rotterdam, Erasmus MC, Rotterdam, where he is heading the "Image Guidance in Interventions and Therapy" theme group, which focuses on improving image guidance by integrating pre-operative image information in the interventional situation for cardiac and abdominal applications. Challenges addressed are the modeling and tracking of motion and deformation of the target anatomy and the instruments. Additionally, he is involved in cardiovascular image processing, where he co-organized three cardiovascular "Grand Challenges": the coronary artery tracking challenge (coronary.bigr.nl), the carotid lumen segmentation and stenosis grading challenge (cls2009.bigr.nl), and the coronary stenoses detection and quantification challenge (coronary.bigr.nl/stenosis).

Johannes G. Bosch (M'07) is an Associate Professor at the Department of Biomedical Engineering, Thoraxcenter, Erasmus MC, Rotterdam. He is specialized in 2-D and 3-D echocardiographic image processing/analysis and transducer development. His main research interests are optimal border detection approaches, geometrical and statistical models, and anatomical and physical knowledge representations for border detection. He is currently the leader of projects on 3-D segmentation and 3-D ultrasound guidance in electrophysiology and participates in projects on 3-D transducer development, 2-D and 3-D carotid imaging, and 3-D TEE imaging. He obtained his M.Sc. degree in electrical engineering at the Eindhoven University of Technology in 1985. From 1995 to 2005, he was Assistant Professor and head of the Echocardiography section at the Division of Image Processing (LKEB), Department of Radiology, Leiden University Medical Center, where he obtained his Ph.D. degree in 2006.